Experimental and Theoretical Study for Nonlinear Aeroelastic Behavior of a Flexible Rotor Blade

D. M. Tang* and E. H. Dowell†
Duke University, Durham, North Carolina 27706

The purpose of this paper is to study the flutter instability and forced response of a nonrotating flexible rotor blade model with a geometrical structural nonlinearity and a freeplay structural nonlinearity. The ONERA stall aerodynamic model is used. External excitations are provided by base harmonic excitations in the pitch angle and the chordwise direction, respectively. Two cases are considered in this paper. Case A is for a nonlinear blade structure with an unstalled unsteady aerodynamic model. Case B is for the nonlinear blade structure with a large effective mean angle of attack. The effects of the structural and aerodynamic nonlinearities and initial disturbance on instability and forced response behavior are discussed. A wind-tunnel test has also been carried out in the Duke University low-speed wind tunnel. The wind-tunnel tests show generally good agreement between theory and experiment for both static and dynamic behavior. Although the mathematical and experimental model of the nonrotating blade is different from the operational rotating hingeless rotor blade, the results from the experimental-theoretical correlation study provide fundamental understanding of the nonlinear aeroelastic behavior for a flexural-flexural-torsional hingeless rotor blade.

Nomenclature

a_{0l}	= blade section linear lift curve slope
b	= blade semichord, $c/2$
$\bar{b}$	= b/R
C_d	= section drag coefficient
C_l	= section lift coefficient
C_m	= section pitch moment coefficient
c	= blade chord
$\bar{c}$	= dimensionless blade chord
dD, dL	= section drag and lift forces
dF_v, dF_w	= section lag and flap component forces
dM_x	= section pitch moment about elastic axis
dM_0	= section pitch moment about quarter chord
E	= modulus of elasticity
e	= mass centroid of blade section from the elastic axis
G	= shear modulus
g	= gravitational constant
I_1, I_2	= flap, chordwise area moments
J	= torsional stiffness constant
K_m	= blade mass radius of gyration
$K_{\phi s}$	= linear torsional spring constant
k	= reduced frequency, $b\omega/U$
m	= mass per unit length of the blade
N	= total number of modes
NN	= number of aerodynamic elements
R	= rotor radius
t	= time
t_τ	= b/U
U	= freestream velocity
V_j, W_j	= generalized coordinates for bending
v	= chordwise bending deflection, also called lag
v_b	= base excitation amplitude in chordwise direction
v_t	= chordwise deflection at the blade tip
w	= flap bending deflection, perpendicular to v
w_t	= flap deflection at the blade tip
x	= position coordinate along blade span
y_{ac}	= aerodynamic center of section from elastic axis

α	= blade section angle of attack
Δ_l	= dimensionless width of lth aerodynamic section
θ_c	= base excitation amplitude in pitch angle
θ_0	= initial pitch angle
μ	= amplitude ratio of ϕ_L to ϕ_a
ρ	= air density
τ	= reduced time, tU/b
Φ_j	= generalized coordinates for torsion
ϕ	= twist about deformed elastic axis
ϕ_a	= magnitude of dead space in pitch
ϕ_L	= limit cycle amplitude in pitch
ϕ_p	= static deviation pitch angle
ϕ_r	= pitch angle at the blade root
ϕ_t	= pitch angle at the blade tip, $\phi_t = \phi_r + \phi_{te}$
ϕ_{te}	= elastic twist at the blade tip
ϕ_λ	= inflow angle
ω_{xj}	= jth torsional natural frequency of blade
ω_{yj}	= jth lag natural frequency of blade
ω_{zj}	= jth flap natural frequency of blade
$(\ )'$	= $d(\ )/dx$
$(\dot{\ })$	= $d(\ )/dt$

Introduction

THE Hodges-Dowell elastic blade equations[1] provide a nonlinear theory of hingeless rotor blade dynamics. The Princeton beam data[2] are regarded as a benchmark for evaluating the aforementioned nonlinear beam theory and other subsequent theories. A comparison of the experimental data with the Hodges-Dowell theory validates the theory only for small and moderate bending deflections compared with the beam span. In subsequent developments, several investigators modified and improved the nonlinear beam equations that were validated by static and vibration experiments and also stability tests based on model rotor blades.[3-12]

The principal stability problems associated with isolated hingeless or bearingless rotors in hover and forward flight are the coupled flap-lag and flap-lag-torsional instabilities for both rigid and elastic rotor blades. The Hodges-Dowell equations indicate that there is an important structural effect on rotor blade stability due to the nonlinear coupling between elastic flap and chordwise bending and torsion. Reference 13 presented a valuable assessment of the state of the art in aeroelastic stability of the hingeless rotor blades. It is evident from this survey that incorporation of geometrically nonlinear terms in both aeroelastic stability and response analysis prob-

lems has become fairly routine. Moreover, it was asserted that substantial improvements in the aerodynamic model will be much more important than incorporation of higher order geometrically nonlinear terms for the structural model. Therefore, in this study, we retain the essential geometrically nonlinear structural terms from the Hodges-Dowell equations and use the ONERA nonlinear aerodynamic model. In addition to the geometrically nonlinear terms, the freeplay structural nonlinearity of the torsional stiffness due to a loose hinge or linkage of a control system or possible joint slippage in the helicopter control system is also included. The external excitations come from the base harmonic excitations in the pitch angle and the chordwise direction, respectively. Although the mathematical model of the nonrotating blade is different from the operational hingeless rotor blade, the results from the experimental-theoretical correlation study will provide fundamental understanding of the nonlinear aeroelastic behavior for a flexural-flexural-torsional hingeless rotor blade.

Two cases are considered in this paper. Case A is for a nonlinear blade structure with an unstalled unsteady aerodynamic model. Case B is for the nonlinear blade structure with a large effective mean angle of attack and the full ONERA nonlinear aerodynamic model. For the nonlinear stability analysis in case A, a set of first-order perturbation equations in the state vector space is formed and solved as an eigenvalue problem for a linearization of the pitch stiffness. The limit cycle oscillation of the nonlinear system is predicted by a certain analysis scheme. For case B, a direct time integration is used to obtain a time history response solution and to compare with the experimental results. The effects of the structural and aerodynamic nonlinearities and initial disturbance on instability and forced response behavior are discussed. Comparisons of the results for the two cases are helpful in understanding physically the nonlinear aeroelastic phenomena.

A wind-tunnel test has also been carried out in the Duke University low-speed wind tunnel. The experimental model includes two parts: a slender cantilever blade and a root support mechanism. The root support mechanism allows a change in the constraint condition at the support of the pitch spring to obtain the freeplay nonlinear characteristics of the pitch spring as well as to excite the pitch direction motion. Two blade models are used in the experimental investigation. One has a high critical flutter speed for the static deformation study, called model I. The other has a lower critical flutter speed for the dynamic motion study, called model II. The experimental technique used in the present paper is an extension of those described in Ref. 14. The wind-tunnel tests show generally good agreement between theory and experiment for both static and dynamic behavior.

Equations of Motion

The present study is based on a consistently derived system of equations of motion for an elastic hingeless blade model under base harmonic excition in pitch angle or lateral direction for a nonrotating blade as shown in Fig. 1. According to the Hodges-Dowell equations,[1] for a nonrotating uniform, untwisted elastic blade, neglecting cross-sectional warping, the equations of motion may be written as

$$EI_2 v'''' + (EI_2 - EI_1)(\phi w'')'' + m\ddot{v} + v_{mg} = \frac{dF_v}{dx} + f_{bv} \quad (1)$$

$$EI_1 w'''' + (EI_2 - EI_1)(\phi v'')'' + m\ddot{w} + me\ddot{\phi} + w_{mg} = \frac{dF_w}{dx} + f_{bw} \quad (2)$$

$$M_k = \begin{cases} K_\phi[\phi(0, t) - \theta] \\ K_\phi(\phi_p - \phi_a) \\ K_\phi(\phi_p - \phi_a) + K_\phi[\phi(0, t) - \theta] \end{cases}$$
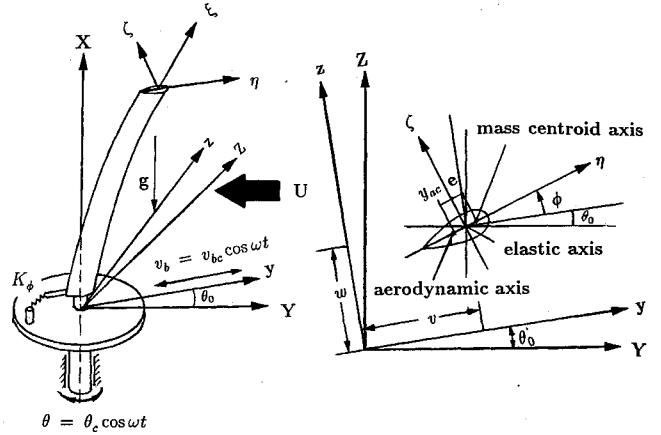

Fig. 1 Physical representation of flexible rotor blade.

$$-GJ\phi'' + (EI_2 - EI_1)w''v'' + mK_m^2\ddot{\phi} + me\ddot{w} + M_k$$

$$= \frac{dM_x}{dx} + m_{bx} \quad (3)$$

Note that in Eqs. (1–3) only the most important nonlinear terms are retained from the Hodges-Dowell equations and the third and higher order geometrically nonlinear terms are neglected here. Also note that ϕ is measured with respect to the deformed elastic axis. For the blade structure with a pitch spring at the root, the torsional motion ϕ includes elastic torsional deformation along the blade span and pitch motion at the blade root.

The vertical longitudinal displacement of the blade is

$$u = -\frac{1}{2}\int_0^x [(v')^2 + (w')^2]\,dx$$

Hence, the gravitational elastic potential energy of the blade is

$$V_{mg} = -\frac{1}{2}mg\int_0^R \int_0^x [(v')^2 + (w')^2]\,dx\,dx$$

and the potential energy from the root spring motion is

$$V_k = \frac{1}{2}K_\phi[\phi(0, t) - \theta]^2$$

The base excitation in the pitch angle and chordwise direction are represented as

$$\theta = \theta_c \cos \omega t$$

$$v_b = v_{bc} \cos \omega t$$

Thus, the incremental kinetic energy corresponding to variables w, v, and ϕ due to the base motion is

$$T_b = m\int_0^R (\dot{v}\dot{v}_b + e\dot{w}\dot{\theta} + K_m^2\dot{\phi}\dot{\theta})\,dx$$

From V_{mg}, V_k, and T_b the restoring stiffness terms v_{mg}, w_{mg}, and M_k and the inertial excitation forces and moment f_{bv}, f_{bw}, and m_{bx} may be deduced by variational methods.

In Eq. (3), M_k is a linear or nonlinear restoring moment that depends on the support conditions of the pitch spring in the experimental model. For the nonlinear freeplay restoring moments vs rotation with a preload (see Fig. 2 of Ref. 15), the moment-rotation relationships can be expressed as

$$[\phi(0, t) - \theta] < (\phi_p - \phi_a)$$

$$(\phi_p - \phi_a) \leq [\phi(0, t) - \theta] \leq (\phi_p - \phi_a) \quad (4)$$

otherwise

The v and w components of the aerodynamic forces and the aerodynamic moment about the elastic axis (see Fig. 1) can be expressed as follows:

$$dF_w = dL - (\phi\lambda - \theta_0)dD$$

$$dF_v = -dD - (\phi\lambda - \theta_0)dL \qquad (5)$$

$$dM_x = dM_0 - y_{ac}dF_w$$

where

$$dL = \tfrac{1}{2}\rho c U^2 C_l \, dx$$

$$dD = \tfrac{1}{2}\rho c U^2 C_d \, dx$$

$$dM_0 = \tfrac{1}{2}\rho c^2 U^2 C_m \, dx$$

$$\phi_\lambda \approx \dot{w}/(U + \dot{v} + \dot{w}\theta_0)$$

$$\alpha = \phi + \theta_0 - \phi_\lambda$$

For the ONERA aerodynamic model, the lift, drag, and moment coefficients of each blade section in the differential equations are described in terms of a reduced time ($d/d\tau$, $\tau = Ut/b$). This time scale is not convenient for the dynamic analysis of the blade, however. A more conventional differential operator relative to the real time d/dt is used in this paper for comparison with the experimental data. This is given by

$$\frac{d}{d\tau} = \frac{b}{U}\frac{d(\ )}{dt} = t_r(\ ^{\cdot}\ )$$

The final form of the ONERA model used for this study incorporates all terms needed such that they fit the well-known theoretical Theodorsen coefficients within the linear small angle of attack domain of rotor blade operation:

$$C_z = C_{za} + C_{zb} \qquad (6)$$

$$C_{za} = t_r s_z \dot{\alpha} + t_r^2 k_{vz} \ddot{\phi} + C_{z\gamma} \qquad (7)$$

$$t_r \dot{C}_{z\gamma} + \lambda_z C_{z\gamma} = \lambda_z(a_{0z}\alpha + t_r\sigma_z\dot{\phi}) + \alpha_z(t_r a_{0z}\dot{\alpha} + t_r^2\sigma_z\ddot{\phi}) \qquad (8)$$

$$t_r^2 C_{zb} + 2t_r dw\dot{C}_{zb} + w^2(1 + d^2)C_{zb}$$

$$= -w^2(1 + d^2)\left(\Delta C_z + t_r e\frac{\partial\Delta C_z}{\partial\alpha}\dot{\alpha}\right) \qquad (9)$$

where C_z represents either the relevant nondimensional lift force coefficient C_l, drag coefficient C_d, and/or the pitch moment coefficient C_m. For the coefficients associated with Eqs. (6–9), see Refs. 16 and 17. The moment is taken about the rotor blade quarter chord.

The ONERA dynamic stall model is based on a blade airfoil element. Here, it is applied to a blade motion problem. A simple assumption is that the blade is divided into several spanwise aerodynamic sections, say NN, and the ONERA model is applied to each section. For the lth blade section, the variables C_{la}, C_{lb}, ..., α, and ϕ_λ should have a subscript l in Eqs. (5–9).

In Eqs. (1–3), expansions in general mode shape functions are used to obtain ordinary differential equations in terms of generalized coordinates. They are expressed in series form as follows:

$$\bar{v} = \sum_{j=1}^{N} V_j(t)\psi_j(\bar{x})$$

$$\bar{w} = \sum_{j=1}^{N} W_j(t)\psi_j(\bar{x}) \qquad (10)$$

$$\phi = \sum_{j=1}^{N} \Phi_j(t)\Theta_j(\bar{x})$$

where $(\bar{\ })$ indicates nondimensionalization with respect to the blade span R, and ψ_j and Θ_j are the jth normal modes of the associated linear problem.

Substituting Eq. (10) into Eqs. (1–3), and using the Galerkin method, one obtains

$$\sum_{j=1}^{N}\left[\delta_{ij}(\ddot{V}_j + \omega_{vj}^2 V_j) - D_{ij}V_j + \beta\sum_{k=1}^{N}K_{jki}\Phi_j W_k\right]$$

$$= -p\sum_{l=1}^{NN}\Delta_l\psi_{il}[C_{dl} + (\phi_{\lambda l} - \theta_0)C_{ll}] + A_i\omega^2\bar{v}_{bc}\cos\omega t \qquad (11)$$

$$\sum_{j=1}^{N}\left[\delta_{ij}(\ddot{W}_j + \omega_{wj}^2 W_j) - E_{ij}\ddot{\Phi}_j - D_{ij}W_j + \beta\sum_{k=1}^{N}K_{jki}\Phi_j V_k\right]$$

$$= p\sum_{l=1}^{NN}\Delta_l\psi_{il}[C_{ll} - (\phi_{\lambda l} - \theta_0)C_{dl}] + A_i\omega^2\bar{e}\theta_c\cos\omega t \qquad (12)$$

$$\sum_{j=1}^{N}\left[\delta_{ij}(\bar{K}_m^2\ddot{\Phi}_j + \bar{K}_m^2\omega_{\phi j}^2\Phi_j) + E_{ji}\ddot{W}_j + \beta\sum_{k=1}^{N}K_{ijk}V_j W_k\right]$$

$$+ \delta K_e b_i\left(\sum_{j=1}^{N}\Phi_j b_j - \theta\right) = p\bar{c}\sum_{l=1}^{NN}\Delta_l\Theta_{il}\{C_{ml} - \bar{y}_{ac}[C_{ll}$$

$$- (\phi_{\lambda l} - \theta_0)C_{dl}]\} + \omega^2\bar{K}_m^2 B_i\theta_c\cos\omega t \qquad (13)$$

where $i = 1, 2, \ldots, N$, δ is the describing function for the freeplay nonlinearity,[14] δ_{ij} is the Kronecker delta, and the other coefficients are available from the authors upon request.

Experiments

All flutter and forced response tests were performed in the Duke University low-speed wind tunnel. The wind-tunnel test model and measurement system used in this study are similar to those used in Ref. 14. The wind tunnel is a closed-circuit tunnel with a test section of 2.3×1.75 ft^2 and a length of 5 ft. The maximum airspeed attainable is 293 ft/s.

The experimental model includes two parts: a blade section and a root support mechanism. The blade is rectangular, untwisted, and flexible in the flap, lag, and torsional directions. The blade is constructed from an aluminum alloy spar with mass per unit length uniformly distributed along the blade span and eight rigid light wood styrofoam fairing elements covering the entire chord and span that provide the aerodynamic contour of the blade. Each element is attached to the spar independently so that the stiffness of the spars would not be altered. The gap between two neighboring elements is covered by a piece of adhesive tape that allows the blade to be flexible in both the bending and torsional directions.

There are two experimental models with different parameters and boundary conditions at the blade root, called model I and model II. Model I is fully clamped at the root and has the higher flutter critical speed. This model is used to study nonlinear static deflections. Differing from model I, model II is constrained by a pitch spring at the root and has the lower flutter critical speed. This latter model is for investigation of nonlinear dynamic behavior.

The root mechanism is mounted to a very heavy support frame that is attached to the ground. The root support mechanism allows the blade to have pitch motion degrees of freedom without flap and lag motion at the root. The pitch axis of the blade is supported on upper and lower bearings in a blade root socket and is free to move in the pitch direction. The pitch spring uses a steel wire spring material. The steel wire is inserted tightly into a slot of the blade root socket. According to the different constraint condition at the support of the pitch spring in the experimental model, two different pitch stiffness characteristics were obtained. When the support at the end of the pitch spring is allowed to have rotation and slip motions without transverse motion, the linear pitch stiffness is obtained. When the support point has a transverse gap, the freeplay structural nonlinearity is obtained, and the magnitude of the dead space can be adjusted. The natural frequency

of the pitch motion can be adjusted by moving the support position of the pitch spring (wire spring). The effective mean pitch angle θ_0 can be adjusted by rotating the root support mechanism. The pitch excitation is driven using an electric motor with variable speed through a cam. The driving frequency and amplitude can be adjusted.

Two axial gauges (flap and lag) for bending modes and a 45-deg gauge for torsional modes were glued to the spar to measure the bending-torsional deflections of the blade tip. Signals from the strain gauges were conditioned and amplified before their measurement through a gauge conditioner and a low-pass filter. The positions of the strain gauges along the blade span are $\bar{r} = 0.04$ and 0.29 for bending modes and $\bar{r} = 0.08$ and 0.33 for torsional modes. The pitch angular displacement is also measured by a rotational velocity/displacement transducer (RVDT). The pitch and lateral displacement driving frequency and amplitude are measured by the RVDT, which is mounted to the ends of the pitch driving axis, and an accelerometer, which is mounted on the shake table. The output signals from these strain gauges and transducers were amplified and recorded on a multiple channel tape recorder or directly recorded on a signal analyzer, SD 380. The digitized response data may be displayed as a time history or fast Fourier transform (FFT) and/or power spectral density (PSD). The digitized time history information is also downloaded to the data storage of an IBM pc for plotting the phase plane plots and PSD from the digitized time series.

The measurement system calibration was completed before the wind-tunnel test. The static calibration coefficient is defined as the blade rotation angle ϕ or deflections w and v at the blade tip, divided by the output voltage of the measurement system (from the strain gauges or RVDT to the recorder). The sensitivity of the strain gauge was found to be linear in the operational range and the calibration factors for the strain gauge reading were in microinches/inch of strain per volt. The relationship for strain-tip displacement w_t and v_t or strain-tip rotation angle ϕ_{te} was determined using a static test. Measurements of the blade tip deflection were obtained using those relationships and the output voltages from the strain gauges. For the dynamic test, a strain gauge conditioner was used. The dynamic calibration coefficients were determined by a ground vibration test. The latter dynamic calibration assumes that there is no significant coupling between either of the two bending directions or torsion. This is a reasonable assumption for the present test configuration.

Several of the parameters of the experimental model are obtained by test. The flexible flap, lag, and torsional stiffnesses EI_1, EI_2, and GJ of the model are determined from a static test. The first few natural frequencies and mode shapes of the blade were calculated using the previous stiffnesses and measured using a general vibration test (hammer test). Results from the test were slightly higher than those from the calculation by about 3–5%. This is probably due to hysteretic behavior of the model blade. The hammer vibration test usually has a small excitation force and leads to a higher frequency for a specimen with hysteretic behavior. The inertial parameters of each element of the blade sections are measured and checked from the previous test data. The pitch spring constant is

Table 1 Analytic solution procedure

	model I	model II
R, in.	19.68	19.68
c, in.	3.15	3.15
$\bar{c}$	0.16	0.16
ω_z, Hz	7.32	10
ω_y, Hz	39	23.5
GJ, lb-in.^{2}	0.25×10^4	0.25×10^4
m, lb^2/in.^{2}	0.58×10^{-4}	0.47×10^{-4}
K_m, in.	1.0126	1.149
$K_{\phi s}$, lb-in./rad	—	18.62
$\bar{y}_{am}$	-0.05	-0.1
$\bar{y}_{ac}$	-0.05	-0.05

determined by a static load test. All parameters of the two models are summarized in Table 1.

A. Eigenvalue Stability Solution for Case A

For the unstalled instability problem of case A, the base excitation motions are removed, and the aerodynamic forces and moment coefficients are represented by Eqs. (7) and (8). According to the given aerodynamic coefficients, C_{da} and C_{ma} can be rewritten as

$$C_{da} = C_{d0} + t_\tau s_d \alpha \dot{\alpha}$$
$$C_{ma} = t_\tau s_m \dot{\alpha} + t_\tau \sigma_m \dot{\phi} + t_\tau^2 k_{vm} \ddot{\phi} \tag{14}$$

For the coefficients C_{d0} and σ_0, see Ref. 16, and for s_m, σ_m, and k_{vm}, see Ref. 17.

From Eqs. (14), (7), and (8), it is found that C_{la} and C_{ma} are linear, and C_{da} is nonlinear in terms of α and $\dot{\alpha}$, and also it is found that C_{da} and C_{ma} are explicit functions of α and ϕ, but C_{la} is described as a first-order differential equation that also depends on the position of the aerodynamic element.

The nonlinear structural restoring moment M_k in Eq. (3) can be replaced using an equivalent linearization of the restoring moment $K_{\phi e}[\phi(0, t) - \theta]$, where the equivalent stiffness $K_{\phi e}$ will be discussed subsequently. For a given $K_{\phi e}$, to solve the instability problem of the nonlinear equations, Eqs. (11–13), one must first linearize the equations using a perturbation procedure. The perturbation expansions of each variable lead to a set of homogeneous equations.

The static equilibrium equations are

$$\sum_{j=1}^{N} \left[\delta_{ij} \omega_{vj}^2 V_{0j} - D_{ij} V_{0j} + \beta \sum_{k=1}^{N} K_{jki} \Phi_{0j} W_{0k} \right.$$
$$\left. - p\theta_0 a_{0l} C_{ij} \Phi_{0j} \right] = -pA_i(C_{d0} - \theta_0^2 a_{0l})$$

$$\sum_{j=1}^{N} \left[\delta_{ij} \omega_{wj}^2 W_{0j} - D_{ij} W_{0j} + \beta \sum_{k=1}^{N} K_{jki} \Phi_{0j} V_{0k} \right.$$
$$\left. - pa_{0l} C_{ij} \Phi_{0j} \right] = pA_i \theta_0 (C_{d0} + a_{0l}) \tag{15}$$

$$\sum_{j=1}^{N} \left[\delta_{ij} (\bar{K}_m^2 \omega_{\phi j}^2 \Phi_{0j} + \beta \sum_{k=1}^{N} K_{ijk} V_{0j} W_{0k} + \delta K_e b_i \Phi_{0j} b_j \right.$$
$$\left. + p\bar{y}_{ac} \bar{c} a_{0l} \Phi_{0i} \right] = -p\bar{c} \bar{y}_{ac} B_i \theta_0 (C_{d0} + a_{0l})$$

Equations (15) consist of $3N$ nonlinear algebraic equations in V_{0j}, W_{0j}, and Φ_{0j} that are solved by iteration using the Newton–Raphson method.

The perturbation equations about the static equilibrium condition may be expressed as a matrix equation of first order by

$$\begin{bmatrix} M_{jj} & M_{jl} \\ M_{lj} & M_{ll} \end{bmatrix} \begin{Bmatrix} \Delta \dot{q}_{a1} \\ \Delta \dot{q}_{a2} \end{Bmatrix} = \begin{bmatrix} K_{jj} & K_{jl} \\ K_{lj} & K_{ll} \end{bmatrix} \begin{Bmatrix} \Delta q_{a1} \\ \Delta q_{a2} \end{Bmatrix} \tag{16}$$

where

$$[K] = \begin{bmatrix} [k_{jj}]_{6*6} & | & [k_{jl}]_{6*1} \\ \hline [k_{lj}]_{1*6} & | & [k_{ll}]_{1*1} \end{bmatrix}$$

The matrix $[M]$ has the same form as $[K]$, and

$$\{\Delta q_{a1}\}^T = [\ldots \Delta \dot{V}_j \Delta V_j \Delta \dot{W}_j \Delta W_j \Delta \dot{\Phi}_j \Delta \Phi_j \ldots]$$

$$\{\Delta q_{a2}\}^T = [\ldots \Delta C_{l\gamma l} \ldots]$$

For the coefficients of the matrix $[m_{jj}] \ldots$ and $[k_{jj}] \ldots$ see Ref. 18.

The perturbation equation (16) is a set of $6N + NN$ first-order differential equations with a like number of eigenvalues. Of these values, there are $6N$ roots that are complex conjugate pairs that represent the aeroelastic configuration (V, W, and Φ). The other roots are latent aerodynamic roots. The latter are always stable in this study. When given an equivalent stiffness, the roots are functions of the airspeed U. The critical speed and oscillation frequency can be determined using the Nyquist criterion. When given a series of $K_{\phi e}$, we will obtain an instability boundary of U vs $K_{\phi e}$.

Now, let us discuss the equivalent stiffness, $K_{\phi e}$.

Because there is an initial pitch angle θ_0, in general the NACA 0012 airfoil section is subjected to a preload moment in the freestream velocity field; hence a static angle ϕ_p exists, and the torsional stiffness curve is not symmetric. The static angle is dependent on U, θ_0, and the elastic deflection of the blade. The expression for the static angle is given by

$$\phi_{p+,-} = \sum_{j=1}^{N} \Theta_j(0)\Phi_j(U, \psi_j, \Theta_j, \theta_j \pm \phi_a) \pm \phi_a \qquad (17)$$

where ϕ_p can be obtained by solving the static nonlinear equations of Eq. (14).

The stability problem with freeplay structural nonlinearities is often analyzed through application of a linearization technique, the harmonic balance method or the so-called "describing function" approach. For a nonlinear pitch stiffness with freeplay characteristics, the output waveform is dependent on the magnitude of the freeplay and the amplitude of input displacement. Calculation of the nonlinear spring displacement is usually accomplished through normal mode summation. This approach, however, requires prior knowledge of the normal mode shapes of the system, which are themselves a function of the nonlinear pitch stiffness. Therefore, an amplitude-stiffness alignment becomes necessary for this nonlinear problem. Reference 19 presented an iterative procedure in the frequency domain to accomplish the amplitude-stiffness alignment that is used here.

For the stability problem with a single nonlinear pitch spring, the solution procedure of the nonlinear equation is described as follows.

An equivalent stiffness $K_{\phi e}$ is defined as

$$K_{\phi e} = \delta K_{\phi s} \qquad (18)$$

From Eq. (16), a relationship between the equivalent stiffness $K_{\phi e}$ and the critical speed U is obtained. It is called curve 1. It is well known from Eq. (18) that δ is a function of the amplitude of oscillation as well as freestream velocity. Equations (16–18) are coupled with each other. Assuming a velocity U_1, a curve 2 of $K_{\phi e}$ vs ϕ_L can be drawn using Eqs. (16) and (17). Substituting U_1 into curve 1, an equivalent stiffness $K_{\phi e1}$ is obtained. According to $K_{\phi e1}$, a limit cycle amplitude ϕ_{L1} is found from curve 2. Therefore, the value U_1 with ϕ_{L1} is a solution of the nonlinear equations. Repeating the preceding process for other U called U_i ($i = 1, 2, 3...$), a final graph is drawn of critical speed of instability vs the limit cycle oscillation amplitude at the root as well as at other spanwise positions of the blade.

B. Time History Response Solution for Case B

The time history response solution is used to study the instability motion behavior, stall response, and effects of the initial disturbance at high effective mean angle of attack for case B. Equations (11–13) are second-order, nonlinear differential equations in the variables V_j, W_j, and Φ_j, respectively. Two state variables are required for each jth variable. Equations (8) and (9) together represent a third-order system for the lift coefficient and a second-order system for both drag and pitch moment coefficients. Thus, seven state variables are required per aerodynamic section. The total number of state variables is $6N + 7NN$. The following state vector is introduced into Eqs. (2–5) and Eqs. (11–13), which serves to reduce the system to a set of $6N + 7NN$ first-order differential equations.

Let

$$\{q_b\} = \begin{Bmatrix} q_{bj} \\ q_{bl} \end{Bmatrix} \qquad (19)$$

where

$$\{q_{bj}\}^T = [\ldots \dot{V}_j V_j \dot{W}_j W_j \dot{\Phi}_j \Phi_j \ldots]$$

$$\{q_{bl}\}^T = [\ldots \dot{C}_{lbl} C_{lbl} C_{lyl} \dot{C}_{dbl} C_{dbll} \dot{C}_{mbl} C_{mbl} \ldots]$$

The resulting system of the state variable equations is given by

$$\begin{bmatrix} \hat{M}_{jj} & \hat{M}_{jl} \\ \hat{M}_{lj} & \hat{M}_{ll} \end{bmatrix} \begin{Bmatrix} \dot{q}_{bj} \\ \dot{q}_{bl} \end{Bmatrix} = \begin{bmatrix} \hat{K}_{jj} & \hat{K}_{jl} \\ \hat{K}_{lj} & \hat{K}_{ll} \end{bmatrix} \begin{Bmatrix} q_{bj} \\ q_{bl} \end{Bmatrix} + \begin{Bmatrix} F_j \\ F_l \end{Bmatrix} \qquad (20)$$

or

$$[\hat{K}] = \begin{bmatrix} [\hat{k}_{jj}]_{6*6} & [\hat{k}_{jl}]_{6*7} \\ [\hat{k}_{lj}]_{7*6} & [\hat{k}_{ll}]_{7*7} \end{bmatrix}$$

$$\{F\}^T = [\ldots f_j \ldots | \ldots f_l \ldots]$$

The matrix $[\hat{M}]$ has the same form as $[\hat{K}]$. For the coefficients of the matrix $[\hat{m}_{jj}]\ldots$ and $[\hat{k}_{jj}]\ldots$, $\{f_j\}$, and $\{f_l\}$, see Ref. 18.

The section angle of attack α_l and section inflow angle $\phi_{\lambda l}$ involve the state variables V_j, W_j, and Φ_j. Equations (20) is a set of nonlinear differential equations. The solution of the equations can be obtained by numerical time integration. The initial values of α_l and $\phi_{\lambda l}$ are determined by the initial values of the state variables that then change during the numerical integration in a time step fashion.

Because of the freeplay structural nonlinearity of the pitch spring at the root of the blade, the torsional modes Θ_j are variable with the torsional vibration. During the time integration, only two kinds of pitch spring stiffnesses can be chosen: $\delta = 0$ and 1 from Eq. (13). Therefore, two kinds of torsional modes corresponding to the preceding pitch boundary conditions can be used during the numerical integration and then properly chosen in a time step fashion.

The blade section uses a NACA 0012 airfoil. The static lift and pitch moment coefficients are identified from the experimental data (Ref. 14) using curve fitting. The following results are for the blade divided into four equal length strips with $\Delta_i = 0.25$.

Comparison of Theory and Experiment

A. Static Deflections

In this section, the linear and nonlinear static aerodynamic models are used to calculate static deflections of the blade for comparison with the experimental results for a cantilevered blade model, model I. Geometric structural nonlinearities are included in both theory and experiment. The initial pitch angle θ_0 can be adjusted by rotating the root support mechanism. Measurements of flap and chordwise bending deflection at the blade tip v_t and w_t as well as twist ϕ_{te} have been obtained for several initial pitch angles and for the freestream velocity range $U = 0-31.2$ m/s, which is much lower than the flutter critical speed $U_{cr} = 65.5$ m/s for model I. The equilibrium equations based on a linear static aerodynamic model are represented by Eq. (15). The theoretical results were obtained by taking three modes for each of flapwise, chordwise, and twist deflections. The first mode in the resultant deflection is dominant. The equilibrium equations based on a nonlinear static aerodynamic can be derived from Eqs. (11–13) when the dynamic terms are deleted. In these equations, the C_{ll} and C_{ml} are independent of the spanwise location of the blade but dependent on Φ_{0j}. These are determined by Eqs. (21) and (22). The jth torsional natural frequency for a clamped blade root is $\omega_{\phi j}$. They consist of $3N + 2$ nonlinear algebraic equations in V_{0j}, W_{0j}, Φ_{0j}, and C_{ls}, C_{ms}, which are solved by iteration using the Newton-Raphson method.
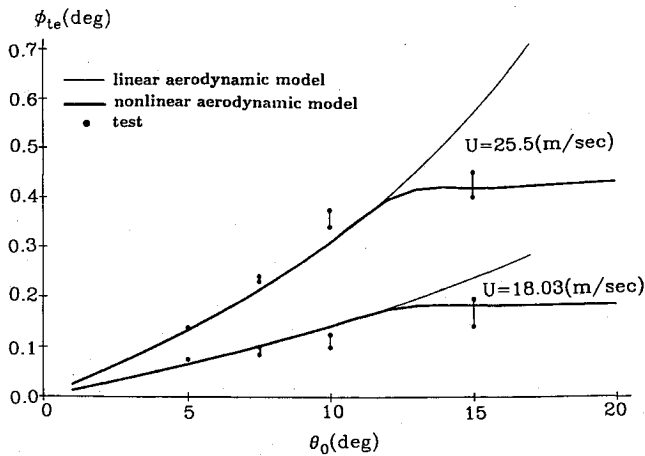
Fig. 2   Static deflections of the twist vs θ_0 for U = 18.03 and 25.5 m/s.

Typical results for static twist vs θ_0 for U = 18.03 and 25.5 m/s are shown in Fig. 2. The theoretical and experimental results are indicated by the thin solid lines (linear aerodynamics), thick solid lines (nonlinear aerodynamics), and the symbol (•), respectively. The agreement between theory and test is substantially improved by the nonlinear aerodynamic theory as compared with the linear aerodynamic theory, especially in the range of higher dynamic pressure.

From the comparison of theory and experiment, the following results are found.

1) The most sensitive indicator of the difference between the linear and nonlinear theoretical models is the twist, especially when large initial pitch angle is considered. The flapwise and chordwise deflections at the blade tip are nearly linear vs dynamic pressure for a given initial pitch angle.

2) When θ_0 is smaller than the static stall angle of attack, α_{st} = 13 deg, the agreement between theory and test is reasonable and the linear and nonlinear aerodynamic models give the same results. When θ_0 is larger than α_{st}, the agreement is somewhat poorer especially in the range of higher dynamic pressure. Note that the linear and nonlinear aerodynamic models give somewhat different results with the latter showing improved agreement with experiment.

3) From the test we also find that there is an irregular oscillation around the static equilibrium position that looks like random motion as $\theta_0 \geq \alpha_{st}$ and U = 25.5 m/s. This oscillation exists in three directions. Comparing the random motion in three directions, the flap motion is dominant. The rms value is about 0.1 (in.). The motions in the chordwise and twist directions are quite small. However, this phenomenon does not occur at small θ_0. This oscillation is induced by unsteady aerodynamic forces when stall occurs. The error bars shown in Fig. 2 reflect the range of dynamic response.

B. Dynamic Behavior

In this section, the ONERA stall aerodynamic model is used to calculate dynamic behavior of the blade for comparison with the experimental results for model II. The lowest flutter critical speed is U_{cr} = 25.7 m/s for the linear system. The lowest critical speed is predicted to occur where the root locus crosses the imaginary axis. The flutter frequency is given by the imaginary axis crossing. The critical speed is 25.7 m/s and flutter frequency is 15.8 Hz. The measured flutter speed is 28.51 m/s and the oscillation frequency is 16.25 Hz. The theoretical results were obtained by taking two modes for each of the flapwise, chordwise, and twist deflections, rather than the three used for the static case, to save computer time. The results still seem well converged based on a few calculations using three modes. For example, the lowest critical speed is 26.1 m/s from theory using three modes. The difference is small between the two and three mode results.

Two major issues are discussed here. One is the effect of geometric structural nonlinearity on the flutter instability and stall response. Another is the effect of freeplay structural nonlinearity on dynamic behavior when stall occurs.

1. Effects of Geometric Structural Nonlinearity

The theoretical calculations for instability are based on the time integration of Eq. (20) when the external forces are removed. Results are shown in Fig. 3 for comparison of the flutter behavior with and without geometric structural nonlinearity, which are called type 1 and type 0, respectively. Figure 3 indicates the flutter limit cycle amplitude of the twist motion and equilibrium position at the tip of blade vs flutter critical speed for θ_0 = 1, 5, and 10 deg. In the figure, the results with and without geometric structural nonlinearity included are indicated by the thin solid lines and broken line, respectively. The symbols of ·, □, and o are for θ_0 = 1, 5, and 10 deg, respectively. The upper boundary of the limit cycle oscillation is indicated by a symbol LC_u and the lower boundary by LC_l in the figure. The following comments can be made.

1) When θ_0 is smaller, such as θ_0 = 1 deg, both systems are stable when $U \leq U_{cr}$. When $U \geq U_{cr}$, both systems tend to a limit cycle oscillation and the amplitude increases as U increases. As the speed increases up to a certain value, the motion will be divergent. The divergence speed is U = 25.1 m/s for type 1 and U = 25.35 m/s for type 0. Both systems have a small range of limit cycle oscillation and the effect of geometric structural nonlinearity is very small.

2) When θ_0 is moderate, e.g., θ_0 = 5 deg, the limit cycle flutter speed is lower than that of the linear system (U_{cr} = 25.7 m/s). It is U_{cr} = 22.5 m/s for type 1 and 23 m/s for type 0. We find that there is a smaller limit cycle oscillation range for type 1, and the divergence speed is 23.2 m/s. However, for the linear structure (type 0), the limit cycle flutter still exists and the divergence speed is 23.7 m/s. The dominant reason for the observed limit cycle is the nonlinear stall aerodynamic model.

3) When θ_0 is larger, such as θ_0 = 10 deg, the limit cycle speed is much lower than that of the linear system. It is U_{cr} = 14 m/s for type 1 and 14.2 m/s for type 0. The divergent speed is U = 16.25 m/s for type 1, and U = 17.3 m/s for type 0. However, the limit cycle amplitude is quite large and not realistic. For such amplitudes, the structure would almost assuredly undergo structural failure.

For comparison with the theoretical results, the experimental results for θ_0 = 5 deg are also plotted in Fig. 3 as indicated by the symbol of $\triangle$. We find a limit cycle flutter oscillation between U = 20.25 and 22 m/s. (The wind speed is limited to the latter value due to the large amplitude and safety concerns.) The measured limit cycle flutter speed is lower than the theoretical result. The experiment, of course, includes geometric structural nonlinearity, i.e., it is type 1.

The theoretical calculations for the forced response are based on the perturbation equations (16) when base harmonic
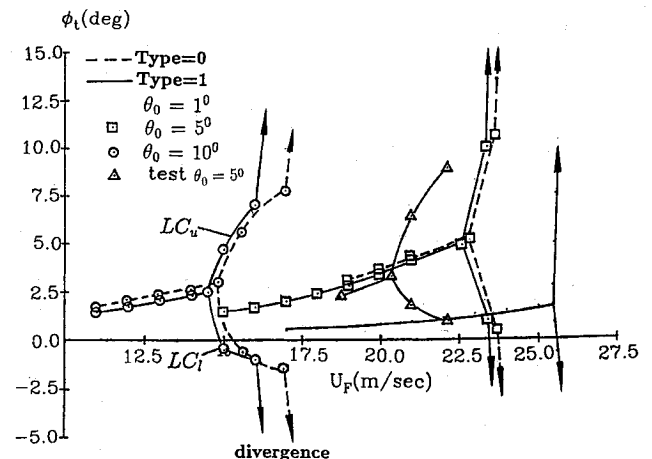

Fig. 3   Effects of geometric structural nonlinearity on stability.

excitations are considered. Thus static nonlinearities are taken into account, but the dynamic response per se is linearized.

The base harmonic excitations in the pitch angle and chordwise direction are generated by a shake table at the root support (the experimental results are only for excitation in the pitch angle). The forced response has the following peculiarities.

For base harmonic excitation only in the pitch angle direction. When θ_0 is smaller, such as $\theta_0 = 1$ deg, the effects of the geometric structural nonlinearity can be almost neglected. When θ_0 is moderate and larger, e.g., $\theta_0 = 5$ and 10 deg, the difference between the linear and nonlinear results is evident, especially near the natural frequencies. This is because the effects of geometric nonlinearity come from the larger structural response and increase as the amplitude increases. The effects of nonlinearity are beneficial for the response amplitude near the first twist natural frequency due to the twist increment and then the aerodynamic force increment. The results of the flap motion are shown in Fig. 4 for $\theta_0 = 1$ deg,
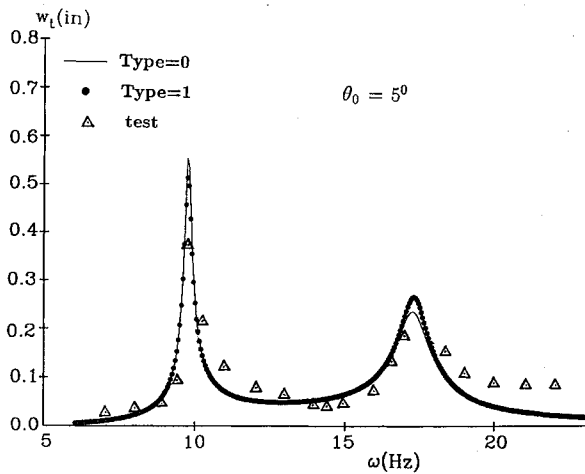
Fig. 4 Effects of geometric structural nonlinearity on forced response in flap direction for $\theta_c = 1$ deg, $\theta_0 = 5$ deg, and $U = 15.6$ m/s.
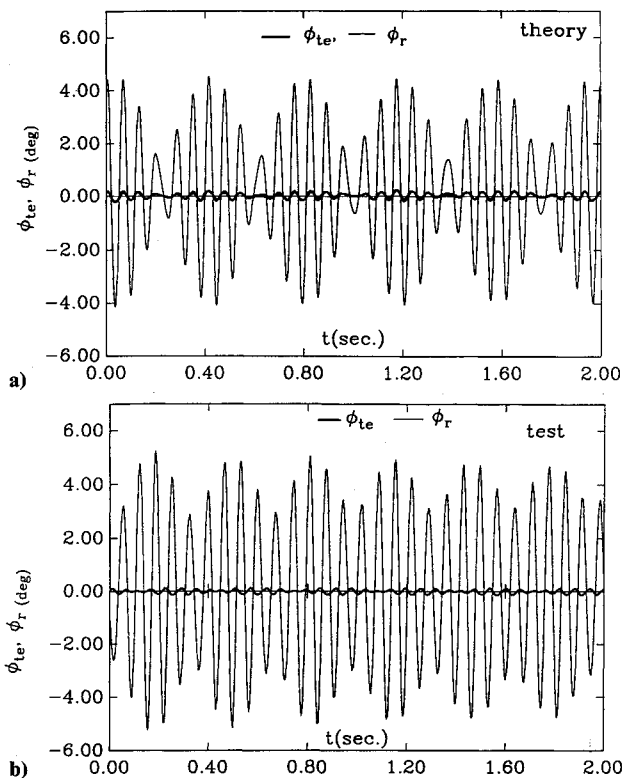

Fig. 5 Time history of pitch response for $\theta_0 = 10$ deg, $\Omega = 14.5$ Hz, and $U = 10.6$ m/s: a) theory, b) test.
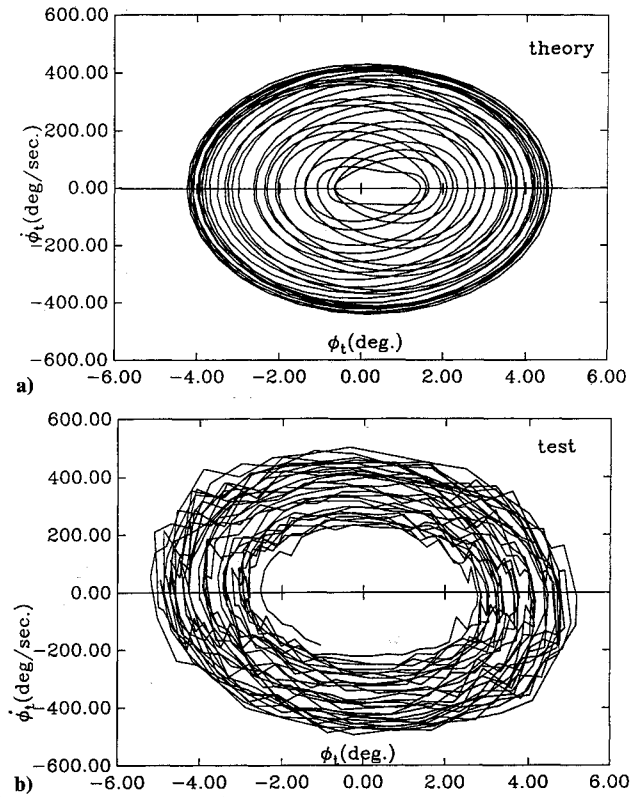

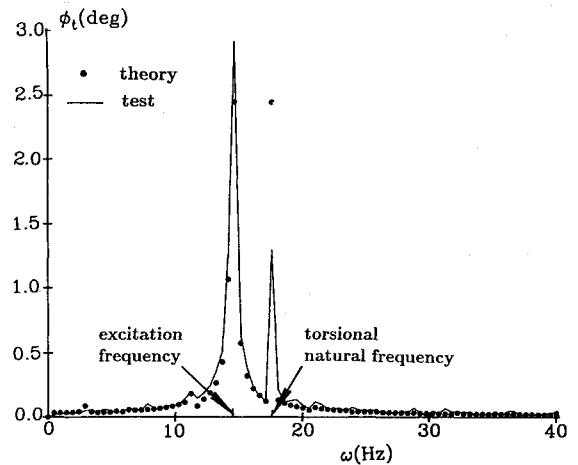Fig. 6 Phase plane plot of pitch response: a) theory, b) test.

Fig. 7 FFT plot of pitch response.

$\theta_c = 1$ deg, and $U = 15.6$ m/s. It is found that the effects of structural nonlinearity on the frequency are substantially larger near the chordwise natural frequency for all of θ_0. The reason comes from the coupling of structural elastic and aerodynamic forces. Also it is found that, in general, the response has a periodic characteristic when θ_0 is less than a certain moderate value. Aperiodic or chaotic response can be found when stall occurs. It will be discussed subsequently.

For comparison with the theoretical results, the measured data for $\theta_0 = 5$ deg are also plotted in Fig. 4 indicated by the symbol of Δ. The larger difference occurs near the first flap natural frequency. There are no test data near the first twist natural frequency $\Omega = 17.2$–18.3 Hz because the twist response amplitude was too large and exceeded the given safety structural constraint in the pitch direction. The measured amplitude is the rms value when the response is aperiodic or chaotic.

A set of typical measured response curves with a comparison with the theoretical results are shown in Figs. 5–7 for the pitch motion at the blade tip. Those figures show the time
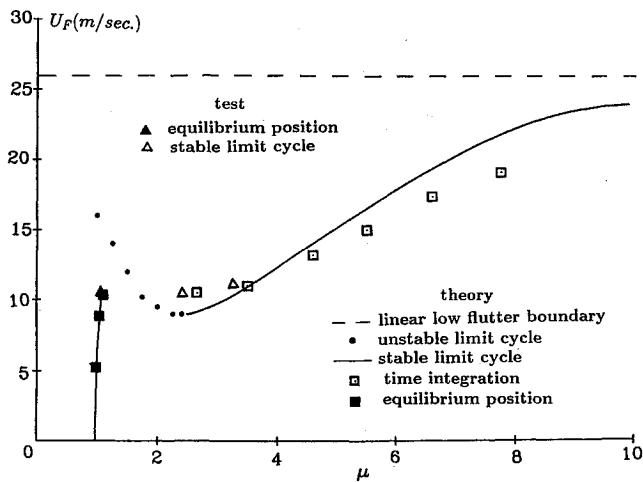
Fig. 8   Flutter speed vs limit cycle amplitude ratio for $\theta_0 = 0$ deg, $\phi_a = 1.5$ deg, and type = 1.
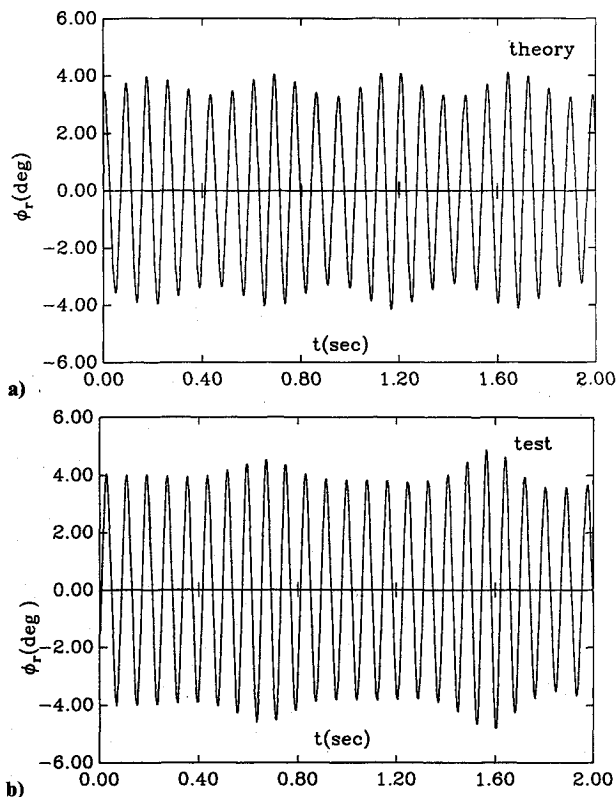

Fig. 9   Time history of pitch motion for $\theta_0 = 0$ deg, $\phi_r(0) = 2$ deg, and $U = 10.5$ m/s: a) theory, b) test.

history and phase plane plot for $\theta_0 = 10$ deg, $\theta_c = 0.5$ deg, $\Omega = 14.5$ Hz, and $U = 10.6$ m/s, respectively. In these figures, a) is the theoretical result and b) is the experimental one. Corresponding to Fig. 5, the FFT plots are shown in Fig. 7. The theory is indicated by the symbol • and experiment by a solid line. The pitch motion is mostly dominated by the first mode. The second mode (elastic deflection) motion is quite small. The agreement between theory and experiment for pitch is generally better than for lag (chordwise response).

For base harmonic excitation only in the chordwise direction. When θ_0 is smaller than a moderate value, the difference of the chordwise response (not shown) between the linear and nonlinear results can be neglected. For the linear system the flap and torsional frequency responses are very small for base excitation in the chordwise direction, when θ_0 is smaller than a moderate value. This is because there is no external

force acting in the chordwise direction. For the nonlinear system, the flap and torsional responses are evident. These responses are induced by the geometric nonlinearity and corresponding aerodynamic forces. The results also show that the dominant response amplitude is near the chordwise natural frequency for all of the w, ϕ, and v response curves. At a certain excitation frequency, the response of the nonlinear structure appears to be aperiodic or chaotic for all w, ϕ, and v motions. It is because the structural nonlinearity leads to a chaotic motion.

2.   Effects of Freeplay Structural Nonlinearity

The theoretical calculations of the instability are based on the time integration of Eqs. (20) and (18) when the external forces are removed. Figure 8 shows the flutter speed vs limit cycle flutter amplitude ratio μ ($\mu = \phi_L/\phi_a$) for the magnitude of dead space in pitch, $\phi_a = 1.5$ deg, $\theta_0 = 0$ deg, and type = 1. In this figure, the theoretical curve is indicated by solid and
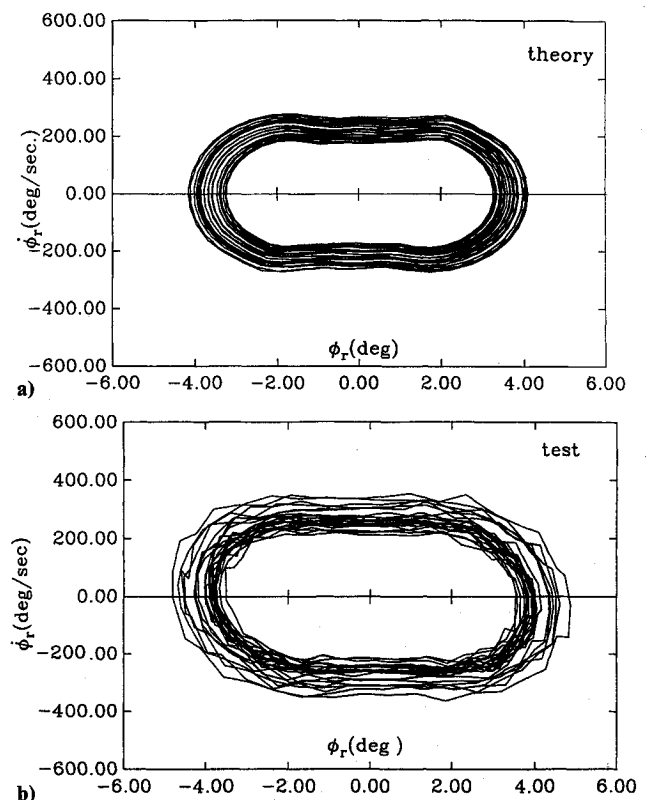

Fig. 10   Phase plane plot of pitch motion for $\theta_0 = 0$ deg, $\phi_r(0) = 2$ deg, and $U = 10.5$ m/s: a) theory, b) test.
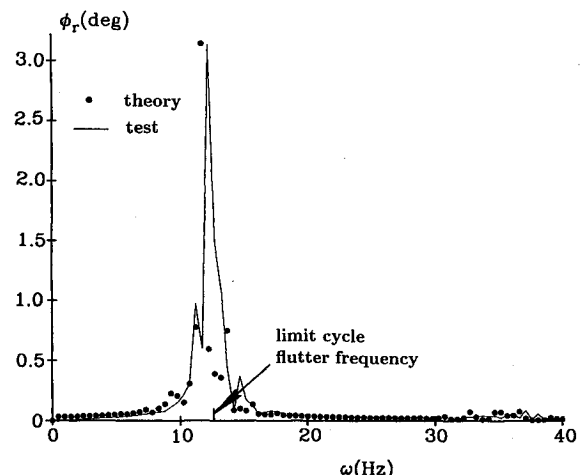

Fig. 11   FFT plot of pitch motion.

dash lines. The solid line denotes stable limit cycle vs airspeed, whereas the dash line denotes unstable limit cycle. The experimental results are indicated by the symbol of $\triangle$. Also, the results obtained from the time integration are plotted in the figure. The symbol of $\square$ denotes that the motion tends to a limit cycle oscillation. The symbols of $\blacksquare$ and $\blacktriangle$ denote that the motion is convergent to a static equilibrium position. The agreement of theory with experiment is good.

An aperiodic oscillation is observed in a narrow airspeed range and for a certain initial condition. It occurs in an amplitude sensitive region. Figures 9-11 show the aperiodic oscillation behavior of pitch motion at the blade root for $\theta_0 = 0$ deg, $\phi_r(0) = 2$ deg, and $U = 10.5$ m/s. Figures 9 and 10 are the time history and phase plane plot, respectively. Figure 11 is the FFT. In these figures, a) is from the theory, and b) is from the experiment. Also, we find a chaotic oscillation around a rest position $\phi_{p+} = 1.6$ deg as shown in Fig. 12. Figure 12 shows the PSD plot of the ϕ_r motion with a comparison between type $= 1$ and type $= 0$ for $U = 9.5$ m/s and $\phi_r(0) = 2$ deg. It is found that more chaotic motion occurs in the case of type $= 1$.

The limit cycle oscillation is quite sensitive to the initial condition and airspeed. As an experimental example of the system sensitivity to the initial condition, in Fig. 8 there are two values of μ for $U = 10.5$ m/s. When the initial pitch angle $\phi_r(0) = 1$ deg, the motion converges to a static equilibrium position. When the $\phi_r(0) > 1.5$ deg, the motion tends to a limit cycle oscillation. Corresponding to the preceding example, the theoretical prediction also exhibits this feature.

Figure 13 shows the limit cycle flutter amplitude of pitch motion at the blade root vs the flutter speed for $\theta_0 = 5$ and 10 deg. The symbol of $\bullet$ denotes the results from the time integra-
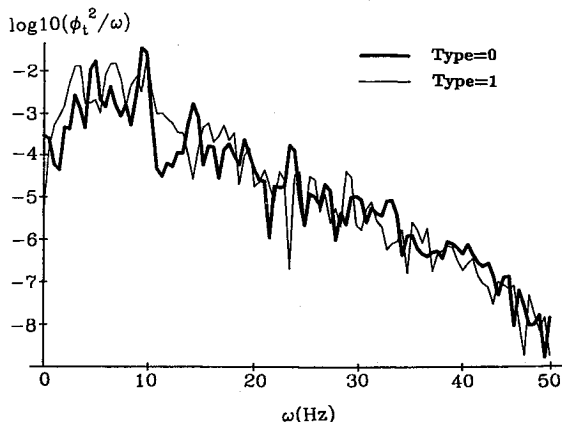

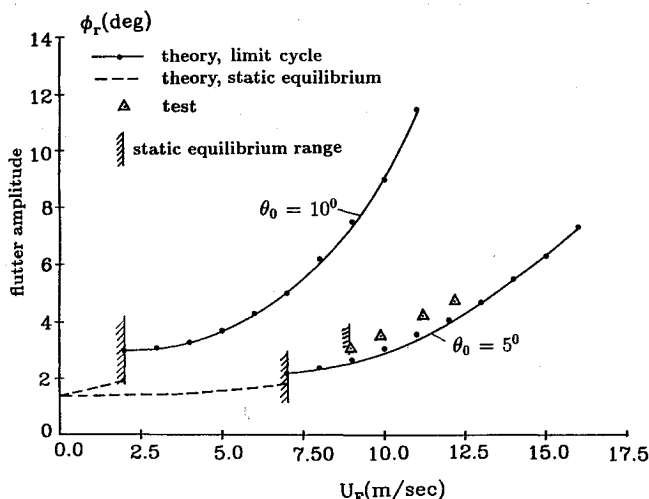Fig. 12 PSD plot of pitch motion.

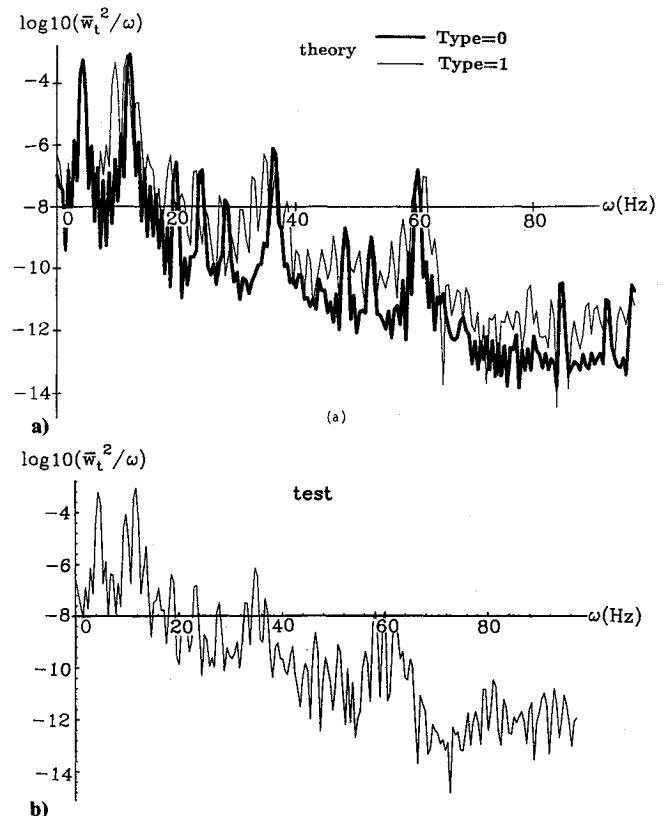Fig. 13 Limit cycle flutter amplitude of pitch motion at the blade root vs flutter speed.

Fig. 14 PSD plot of flapwise response for $\theta_0 = 5$ deg, $\Omega = 4.3$ Hz, $\phi_a = 1.5$ deg, and $U = 9$ m/s: a) theory, b) test.

tion and $\triangle$ from the experiment. The agreement is generally good; however, no experimental limit cycle was observed for U_F below 9 m/s. The theoretical calculations for the forced response are based on Eq. (20) with the external forces included. For base excitation in the pitch angle direction, the forced responses are periodic motions with dominant excitation frequency and higher order frequencies. However, under certain conditions a chaotic response may be found. Figure 14 shows the PSD plot of the flap motion for $\theta_c = 1$ deg, $\Omega = 4.3$ Hz, $\phi_a = 1.5$ deg, $\theta_0 = 5$ deg, $U = 9$ m/s, and zero initial conditions. In this figure, a) is from theory and b) from test. From the PSD plot, in addition to a component corresponding to the excitation frequency, 4.3 Hz, there is a strong frequency component of 11.8 Hz from theory and 11.25 Hz from experiment. This frequency corresponds to the limit cycle flutter frequency of the freeplay nonlinear system. This component is dominant in the response. This is a distinct feature for distinguishing the chaotic behavior of the freeplay system from that for linear forced response. This physical phenomenon also has been observed in the present experiment. The agreement between theory and experiment is reasonably good.

The comparison of PSD response behavior with and without geometric structural nonlinearity is shown in Fig. 14a. It is found that there are many harmonic components in the case of type $= 1$.

From calculation and experiment, we find that when the airspeed and preload θ_0 are lower, the static deviation pitch angle will be small. The effect of geometric nonlinearity can be neglected. The freeplay structural nonlinearity is dominant. When the airspeed and preload θ_0 are higher, the static deviation pitch angle will be large. The freeplay structural nonlinearity is not dominant, and indeed the effect of freeplay can be neglected.

Concluding Remarks

Concluding remarks from the comparison of theory and experiment are as follows.

1) The effects of geometric structural nonlinearity and aerodynamic nonlinearity on both static deflections and dynamic aeroelastic behavior are significant when the initial pitch angle or angle of attack is large or when stall occurs.

2) The freeplay structural nonlinearity will lead to a bounded oscillation (periodic, aperiodic, or chaotic motion), and the initial conditions should be considered as a significant factor.

3) Base excitation in the pitch angle direction can lead to a not small chordwise response when the initial pitch angle is large, and the chordwise motion is more complex than the flap and twist motions. Also, base excitation in the chordwise direction can lead to a not small flap and twist response when the initial pitch angle is large.

4) Theory and experiment display similar phenomena, and the quantitative agreement between theory and experiment is fair to good.

Acknowledgments

References

[1]Hodges, D. H., and Dowell, E. H., "Nonlinear Equations of Motion for the Elastic Bending and Torsion of Twisted Nonuniform Rotor Blades," NASA TN D-7818, Dec. 1974.

[2]Dowell, D. H., Traybar, J., and Hodges, D. H., "An Experimental-Theoretical Correlation Study of Non-Linear Bending Torsion Deformation of a Cantilever Beam," *Journal of Sound and Vibration*, Vol. 50, No. 4, 1977, pp. 535–544.

[3]Hodges, D. H., and Ormiston, R. A., "Stability of Elastic Bending and Torsion of Uniform Cantilever Rotor Blades in Hover with Variable Structural Coupling," NASA TN D-8192, March 1976.

[4]Hodges, D. H., and Ormiston, R. A., "Stability of Hingeless Rotor Blades in Hover with Pitch Link Flexibility," *AIAA Journal*, Vol. 15, 1977, pp. 475–482.

[5]Srinivasan, A. V., Cutts, D. G., and Shu, H. T., "An Experimental Investigation of the Structural Dynamics of a Torsionally Soft Rotor in a Vacuum," NASA CR-177418, July 1986.

[6]Rosen, A., and Friedmann, P. P., "Nonlinear Equations of Equilibrium for Elastic Helicopter or Wind Turbine Undergoing Moderate Deformation," NASA CR-159478, Dec. 1978.

[7]Kaza, K. R., and Kvaternik, R. G., "Nonlinear Aeroelastic Equations for Combined Flapwise Bending, Chordwise Bending, Torsion, and Extension of Twisted Nonuniform Rotor Blades in Forward Flight," NASA TM-74059, Oct. 1977.

[8]Da Silva, C., Marcelo, R. M., and Hodges, D. H., "Nonlinear Flexure and Torsion of Rotating Beams with Application to Helicopter Rotor Blades, I. Formulation," *Vertica*, Vol. 10, No. 2, 1986, pp. 171–186.

[9]Hodges, D. H., Ormiston, R. A., and Peters, D. A., "On the Nonlinear Deformation Geometry of Euler-Bernoulli Beams," NASA TP-1566, May 1980.

[10]Hodges, D. H., "Nonlinear Beam Kinematics for Small Strains and Finite Rotations," *Vertica*, Vol. 11, No. 3, 1987, pp. 573–589.

[11]Minguet, P., and Dugundji, J., "Experiments and Analysis for Composite Blades Under Large Deflections, Part I: Static Behavior," *AIAA Journal*, Vol. 28, No. 9, 1990, pp. 1573–1579.

[12]Minguet, P., and Dugundji, J., "Experiments and Analysis for Composite Blades Under Large Deflections, Part II: Dynamic Behavior," *AIAA Journal*, Vol. 28, No. 9, 1990, pp. 1580–1588.

[13]Friedmann, P. P., "Rotary-Wing Aeroelasticity with Application to VTOL, Vehicles," AIAA Paper 90-1115-CP, April 1990, pp. 1624–1670.

[14]Tang, D. M., and Dowell, E. H., "Comparison of Theory and Experiment for Nonlinear Flutter and Stall Response of a Helicopter Blade," *Journal of Sound and Vibration*, Vol. 162, No. 1, 1993, pp. 1–26.

[15]Tang, D. M., and Dowell, E. H., "Flutter and Stall Response of a Helicopter Blade with Structural Nonlinearity," *Journal of Aircraft*, Vol. 29, No. 5, 1992, pp. 953–960.

[16]Petot, D., "Differential Equation Modeling of Dynamic Stall," *Recherche Aerospatiale*, Vol. 5, No. 5, 1989, pp. 51–64.

[17]Dunn, P., and Dugundji, J., "Nonlinear Stall Flutter and Divergence Analysis of Cantilevered Graphite/Epoxy Wings," *AIAA Journal*, Vol. 30, No. 1, 1992, pp. 153–162.

[18]Lee, C. L., "An Iterative Procedure for Nonlinear Flutter Analysis," *AIAA Journal*, Vol. 24, No. 5, 1986, pp. 833–840.

[19]Tang, D. M., and Dowell, E. H., "Experimental and Theoretical Study for Nonlinear Aeroelastic Behavior of a Flexible Rotor Blade," *Proceedings of AIAA/ASME/ASCE/AHS/ASC 33rd Structures, Structural Dynamics, and Materials Conference*, AIAA, Washington, DC, 1992, pp. 1324–1339, (AIAA Paper 92-2253).